Author/s:
Wang, S;Ashokan, A;Balendhran, S;Yan, W;Johnson, BC;Peruzzo, A;Crozier, KB;Mulvaney, P;Bullock, J

Title:
Room Temperature Bias-Selectable, Dual-Band Infrared Detectors Based on Lead Sulfide Colloidal Quantum Dots and Black Phosphorus

Date:
2023-06-27

Citation:
Wang, S., Ashokan, A., Balendhran, S., Yan, W., Johnson, B. C., Peruzzo, A., Crozier, K. B., Mulvaney, P. & Bullock, J. (2023). Room Temperature Bias-Selectable, Dual-Band Infrared Detectors Based on Lead Sulfide Colloidal Quantum Dots and Black Phosphorus. ACS Nano, 17 (12), pp.11771-11782. https://doi.org/10.1021/acsnano.3c02617.

Room temperature bias-selectable, dual-band infrared detectors based on lead sulfide colloidal quantum dots and black phosphorus

Shifan Wang[1], Arun Ashokan[2], Sivacarendran Balendhran[3,6], Wei Yan[1], Brett C. Johnson[4], Alberto Peruzzo[5], Kenneth B. Crozier[1,3,6], Paul Mulvaney[2], James Bullock[1,*]

(1) Department of Electrical and Electronic Engineering, University of Melbourne, VIC 3010, Australia

(2) ARC Centre of Excellence in Exciton Science, School of Chemistry, The University of Melbourne, VIC 3010, Australia,

(3) School of Physics, University of Melbourne, VIC 3010, Australia,

(4) School of Science, RMIT University, Melbourne, VIC 3001, Australia,

(5) Quantum Photonics Laboratory and Centre for Quantum Computation and Communication Technology, RMIT University, Melbourne, VIC 3000, Australia,

(6) ARC Centre of Excellence for Transformative Meta-Optical System (TMOS), The University of Melbourne, VIC 3010, Australia,

** corresponding author: James Bullock (james.bullock@unimelb.edu.au)*

Abstract

A single photodetector capable of switching its peak spectral photoresponse between two wavelength bands is highly useful, particularly for the infrared (IR) bands, in applications such as remote sensing, object identification, and chemical sensing. Technologies exist for achieving dual-band IR detection with bulk III-V and II-VI materials, but the high cost and complexity as well as the necessity for active cooling associated with some of these technologies precludes their widespread adoption. In this study, we leverage the advantages of low-dimensional materials to demonstrate a bias-selectable dual-band IR detector that operates at room temperature using lead sulfide colloidal quantum dots and black phosphorus nanosheets. By switching between zero and forward bias, these detectors switch peak photosensitive ranges between the mid- and short-wave IR bands with room temperature detectivities of 5×10^{9} and 1.6×10^{11} cm $Hz^{1/2}$ W^{-1}, respectively. To the best of our knowledge, these are the highest reported room temperature values for low-dimensional material dual-band IR detectors to date. Unlike conventional bias-selectable detectors, which utilize a set of back-to-back photodiodes, we demonstrate that under zero/forward bias conditions the device's operation mode instead changes between a photodiode and phototransistor, promising additional functionalities that the conventional structure cannot provide.

Key words: Infrared photodetectors, 2D materials, Colloidal quantum dots, Bias-selectable devices, Room temperature operation

Introduction

Infrared (IR) detection technologies are subject to a fast-expanding application space, spanning communication, computing, imaging and sensing.[1, 2] Among this broadening application space are use-cases which call for IR photodetectors capable of sensing multiple properties of IR light. For example, recent studies have demonstrated single IR detectors capable of obtaining intensity information at different polarisation,[3-5] or discriminating intensity in multiple IR spectral bands.[6-10] The latter of these have attracted significant interest for fields such as multi-band imaging, remote sensing, temperature/flame detection, spectral reconstruction and object identification.[11] The simplest form, known as 'two-colour' or 'dual-band' detectors, is typically achieved by stacking two IR photodiodes in a tandem or back-to-back structure.[1] Photoresponse from the two photodiodes can either be accessed simultaneously, requiring at least three electrodes; or sequentially by using a bias-selectable mode of operation, with only one pair of electrodes. The bias-selectable approach has the advantage of a simpler fabrication process, as well as the requirement of only one bump contact/readout circuit per unit cell.[1] To date, most dual-band IR detectors are fabricated using bulk III-V and II-VI compound material absorbers, most prominently mercury cadmium telluride (MCT or HgCdTe), and indium arsenide (InAs) alloyed with gallium (Ga) or antimony (Sb). Example devices are included in Table 1. However, such materials suffer from high fabrication cost and complexity, the need to consider lattice matching, surface passivation and high noise at room temperature.[12] Therefore, continuous effort has been made in seeking device architectures and materials which overcome some of these limitations, such as quantum-well IR photodetectors,[13, 14] type-II superlattice photodetectors,[15, 16] and more recently the use of low-dimensional materials in quantum dot IR photodetectors,[17-19] and two-dimensional material IR photodetectors.[20]

Low-dimensional materials offer several potential advantages for IR detection. For example, colloidal quantum dots (CQDs) can be synthesised using low-cost solution-based approaches and have been shown to be compatible with established complementary metal oxide semiconductor (CMOS) technologies.[21, 22] CQDs also have advantageous optoelectronic properties, such as strong light absorption, multiexciton generation,[23] size-tuneable bandgaps[24] and reduced Auger processes compared to bulk materials which enable higher operating temperatures.[25, 26] Recent studies have explored PbS,[22, 27-30] PbSe,[31] Ag_2Se,[32] HgSe,[33] HgS[34] and HgTe CQDs[35, 36] for IR detection. Among these, PbS, which is typically used for detection in the short-wave IR (SWIR λ= 1.4 to 3 μm), has significant promise, as evidenced by the recent development of commercially available high resolution SWIR cameras which utilise PbS CQDs.[37] Similarly, two-dimensional (2D), or van der Waals, materials can be transferred onto arbitrary substrates and easily stacked in vertical heterostructures due to their out-of-plane van der Waals bonding.[38] Furthermore, the low volume-dependent thermal noise and thickness-tuneable bandgap, as well as the high quantum efficiencies and carrier mobilities commonly exhibited in 2D materials are all advantageous in IR photodetection.[20, 38] To date, several 2D materials have been incorporated as absorbers in IR sensing systems including graphene,[20, 38] Te,[39, 40] $PtSe_2$,[41-43] $MoTe_2$[44, 45], $ZrGeTe_4$,[46, 47] black phosphorus (bP) and black phosphorus arsenic (bPAs).[48, 49] Some of these 2D materials (*e.g.* graphene and Te), and their heterocontact materials (*e.g.* MoS_2), have already been demonstrated in wafer-scale applications,[22, 50, 51] suggesting others could also be scaled up with further development. Among the various 2D IR materials, bP has drawn significant attention as an emerging material for mid-wave IR (MWIR λ = 3 to 5 μm) applications.[3, 49, 52-56] At thicknesses above 10 layers, bP exhibits its bulk bandgap of ~0.31 eV, which increases through the SWIR and visible region for thinner layers.[57, 58] Black phosphorus also exhibits high mobilities and strong

optical anisotropy, enabling devices with short response times and polarisation sensitivity, respectively.

Motivated by the above advantages, and by the compatibility of CQDs and 2D materials, several teams have developed IR detectors utilising one or both of these material families, yielding excellent results. For example, several groups have incorporated IR CQDs, such as PbS, PbSe and HgTe, with 2D materials, such as MoS_2 and graphene, in sensitised phototransistor devices, yielding high responsivities above 10^3 A/W in the IR.[27, 35, 59] More specific to dual-band detection, Tang *et al*. have developed a SWIR/MWIR CQD photodetector by stacking different-sized HgTe QDs in a back-to-back diode configuration.[36] Others have also explored the combination of bP and MoS_2 with $MoTe_2$ or traditional bulk silicon to enable dual-band IR detection.[60, 61] These more recently developed dual-band detectors using low-dimensional materials are also included in Table 1.

In this work, we extend this research field, demonstrating a bias-selectable dual-band IR detector based on the combination of PbS CQDs with black phosphorus (henceforth referred to as a PbS CQD/MoS_2/bP dual-band detector). We demonstrate that this mixed-dimensional device switches between two detection mechanisms. Earlier studies have demonstrated the advantages of 2D material photodetectors which switch between detection mechanisms,[62-64] including infrared detectors based on $MoTe_2/VO_2$ and WSe_2/VO_2, which utilise the phase change of VO_2.[62, 63] In this study we show the device behaves as a PbS CQD/MoS_2 phototransistor (spectral response peak in the SWIR, centred around $\lambda = 1.45$ μm) under forward bias, or as a bP/MoS_2 photodiode (spectral response peak in the MWIR, up to $\lambda = 4$ μm) under zero bias, respectively, allowing SWIR/MWIR dual-band IR detection. This architecture has an advantage in some applications over existing dual-

band IR approaches as the use of a SWIR phototransistor introduces significant photoconductive gain. Importantly, low-dimensional material photodiodes and phototransistors have both been incorporated with CMOS read-out chips, suggesting a potential technological pathway forward.[22, 65] At the end of this study, we show the application prospects of the detector by demonstrating a SWIR/MWIR imaging system. Hence, this work serves as a promising demonstration of mixed dimensional dual-band IR photodetectors which can modulate their peak spectral response, and detection mechanism, by switching between zero and forward bias.

Result and discussion

A conceptual schematic of the PbS CQD/MoS_2/bP dual-band detector is shown in Figure 1a. It consists of a bP/MoS_2 heterojunction sensitised with a thin layer of PbS CQDs and contacted via two metal electrodes formed on the bP and MoS_2 flakes. The detection mechanism of this two-terminal device depends on the biasing conditions, as illustrated in Figure 1b and 1c. When the detector is under zero bias with no dark current, only the bP/MoS_2 photodiode contributes to the photoresponse, and the device simplifies to that of Figure 1b with the photocurrent given by the short circuit current I_{SC} of the bP/MoS_2 photodiode. When under forward bias and an appreciable dark current flows, the forward-biased bP/MoS_2 heterojunction contributes negligibly, and instead the photoresponse is dominated by the PbS CQD/MoS_2 phototransistor. Illustrative band diagrams explaining these detection mechanisms can be found in the Supplementary Information Figure S1. When under reverse bias, both the photodiode and phototransistor mechanisms can contribute. That is, in addition to the photocurrent collected from the reverse-biased bP/MoS_2 heterojunction, the non-zero current flowing under reverse bias leads to a contribution from the PbS CQD/MoS_2 phototransistor as well. Figure 1d shows the absorption/absorbance spectra of bulk MoS_2,

dispersed PbS CQDs and bulk bP. It can be seen that MoS_2 only absorbs wavelengths $\lambda < 800$ nm,[66] and that PbS CQDs absorb from visible to SWIR with a cut-off dependent on the CQD size (*e.g.* ~6 nm PbS CQDs have a cut-off $\lambda \approx 1.5$ μm).[67] Lastly, bulk bP has a cut-off wavelength $\lambda \approx 4$ μm, in the MWIR region. Hence, the PbS CQD/MoS_2/bP device can be used as a bias-selectable, dual-band detector whose photoresponse originates predominantly from the PbS CQD/MoS_2 phototransistor (up to SWIR) or the bP/MoS_2 photodiode (up to MWIR), under forward or zero bias, respectively.

To investigate this hybrid device concept, a series of three devices was fabricated: a bP/MoS_2 photodiode, a PbS CQD sensitised MoS_2 phototransistor, and a PbS CQD/MoS_2/bP dual-band device. A detailed description of the fabrication procedures is given in the Experimental Section. Briefly, MoS_2 and bP flakes were mechanically exfoliated from bulk crystals onto Si/SiO_2 substrates. Heterojunctions were then formed by transferring the MoS_2 flakes, using a poly(methyl methacrylate) (PMMA) based dry transfer technique, atop the bP flakes. Source-drain electrodes for contacting MoS_2 and bP flakes were then defined by electron beam lithography with metal deposited by electron beam evaporation. Following the contact deposition, PbS CQDs were spin coated onto devices from solution, creating a continuous film of CQDs across the whole substrate <60 nm thick. We note that this continuous CQD film does not short source and drain contacts. This was checked by depositing identical CQD films on bare source and drain contacts (*i.e.* without bP and MoS_2), and confirming that there was no measurable current under bias. Representative images of these three devices are shown in Figure 2a, 2b and 2c. The photoresponse spectra of the individual devices, measured using a custom-built, Fourier-transform infrared (FTIR) photodetector characterisation platform (full details given in the Experimental Section), are shown in Figure 2d, 2e and 2f. Spectra obtained from each of these devices under forward bias $V_{DS} = +0.3$

V (top), zero bias V_{DS} = 0 V (middle), and reverse bias V_{DS} = -0.3 V (bottom) are individually scaled to better show their spectral shapes. The photoresponse of the bP/MoS_2 photodiode, in Figure 2d, covers a wide wavelength range up to $\lambda \approx 4$ μm with a relatively flat response at higher photon energies under zero bias. The photoresponse is enhanced by reverse biasing the photodiode and suppressed by forward biasing, as expected from a photodiode. The same information for a PbS CQD/MoS_2 phototransistor is presented in Fig. 2e. Unlike the photodiode, the photoresponse spectra has a peak centred around $\lambda \approx 1.45$ μm under $V_{DS} = \pm 0.3$ V, but has no observable response at zero bias. This peak is characteristic of the absorption spectra of PbS CQDs with diameters of ~6 nm.[67] Substituting PbS CQDs with other sensitiser materials, such as PbSe CQDs, is found to modify the spectrum shape and wavelength range (see Figure S2 of the Supplementary Section 2). A significant photoresponse is only seen for the PbS CQD sensitised MoS_2 phototransistor when an appreciable current is flowing through the MoS_2 layer, as expected for a phototransistor. Finally, Figure 2f shows the photoresponse spectra of the PbS CQD/MoS_2/bP detector under the three biasing conditions. The photoresponse spectra can be clearly seen as an almost perfect superposition of the response from the PbS CQD/MoS_2 phototransistor and the bP/MoS_2 photodiode in each bias condition. This validates the above-described bias-selectable modes of operation, *i.e.* under zero and forward bias the photoresponse is produced exclusively by the bP/MoS_2 photodiode and PbS CQD/MoS_2 phototransistor, respectively. Similar spectral behaviour is seen for a three-terminal version of this device, whereby the MoS_2 layer is contacted by two separate electrodes, allowing simultaneous detection at the expense of increased complexity (see Figure S3 of the Supplementary Information).

A representative PbS CQD/MoS_2/bP dual-band device is further characterised with greater V_{DS} bias granulation to form a photoresponse map in Figure 3a. The two modes of operation can

be clearly seen whereby the device is predominantly sensitive to SWIR light for forward $V_{DS} > 0.2$ V, which is extended into the MWIR for V_{DS} between -0.2 V and 0 V. Figure 3b provides the spatially resolved photoresponse of a representative PbS CQD/MoS_2/bP dual-band device using laser-beam induced current (LBIC) measurements. Note that this device is the same as that presented in Figure 2b, but with an additional PbS CQD coating. The photocurrent is extracted under two test conditions: *i.* bias of $V_{DS} = 0.3$ V, and illumination at a wavelength of $\lambda = 1.31$ μm; and *ii*. bias of $V_{DS} = 0$ V, and illumination at a wavelength of $\lambda = 1.64$ μm. The blue and red regions that overlay a greyscale microscope image indicate the strength of the measured photoresponse under conditions *i* and *ii*, respectively. It can be clearly seen that photocurrent is generated mainly in the MoS_2 region under condition *i*, where the illumination wavelength at $\lambda = 1.31$ μm is well aligned to the excitonic absorption peak of the PbS CQD. Conversely, the photocurrent is generated in the vicinity of the bP/MoS_2 heterojunction in condition *ii* when the illumination wavelength is $\lambda = 1.64$ μm, due to the fact that this wavelength is beyond the absorption edge of the PbS CQDs. In addition, the linear polarisation-dependent photocurrent measured under the two operation modes is provided in the normalised polar plots of Figure 3c and 3d. In Figure 3c, the photocurrent at $\lambda = 3$ μm is plotted, measured with a bias of $V_{DS} = 0$ V, showing a strong dependence on polarisation angle. This is expected as the photodetection arises from absorption in bP which has an anisotropic crystal structure.[3] In contrast, Figure 3d shows no dependence between photocurrent and linear polarisation angle at $\lambda = 1.31$ μm, when measured with bias of $V_{DS} = 0.3$ V. This occurs as photodetection in this mode comes from the PbS CQD films which do not exhibit linear dichroism. This behaviour introduces another potential functionality of these bias-selectable photodetectors, which if able to rotate, could provide both polarisation and spectral

information. The photoresponse map and polarisation dependence presented in Figure 3 both validate the theory of bias-selectable switching of photodetection modes in this device.

Next, we perform a suite of room temperature characterisation on the PbS CQD/MoS_2/bP device under illumination at two wavelengths: $\lambda = 1.31$ and $\lambda = 2.2$ μm. Figure 4a and 4b show the I-V characteristics of a typical PbS CQD/MoS_2/bP detector, under $\lambda = 1.31$ and 2.2 μm, respectively. The dark I-V curve shows a rectifying behaviour typical of other bP/MoS_2 heterojunctions.[3] For reference, dark I-V behaviour with and without the CQD layer, is provided in the Supplementary Section 4, showing only minor change after the CQD deposition. In Figure 4a (illuminated by $\lambda = 1.31$ μm), the current increases symmetrically around 0 V due to a reduction in the channel resistance by a photogate effect from the PbS CQD layer. The PbS CQDs absorb light and generate photocarriers, with positively-charged carriers being trapped in the layer, resulting in a photogating effect which reduces the MoS_2 channel resistance.[68] In contrast, the I-V characteristics under $\lambda = 2.2$ μm, shown in Figure 4b, exhibit typical photodiode behaviour. That is, the rectifying curve shifts down, resulting in the formation of a short circuit current (I_{SC}) and an open circuit voltage (V_{OC}). This downward shift is not present in Figure 4a, which further supports our physical interpretation of the operating mechanisms. A simplified device model, based on a series connected photodiode and phototransistor, is also developed in the Supplementary Section 5, which qualitatively matches the measured behaviour under these two illumination conditions. Figure 4c and 4d explore the linearity of a representative device by plotting photocurrent against the incident optical power density under the same two illumination wavelengths. In Figure 4c, the PbS CQD/MoS_2/bP device is forward biased ($V_{DS} = 0.3$ V) with illumination ($\lambda = 1.31$ μm). The photocurrent (I_{ph}) linearly increases with optical power density ($I_{ph} \propto P^1$) at low irradiance. However, above 10^{-3} W cm^{-2} it shows a sub-linear trend where $I_{ph} \propto$

$P^{0.3}$. This behaviour is in agreement with other sensitised phototransistors involving CQDs reported in the literature, and is typically attributed to an increase in recombination rate at high excess carrier concentrations or decrease in photoconductive gain related to trap-saturation at high irradiance.[69, 70] Conversely, when the device is under zero bias (V_{DS} = 0 V) with illumination at λ = 2.2 μm, the photocurrent versus incident optical power density relationship remains linear (*i.e.* P^1) for a broader range, as shown in Figure 4d. The broad dynamic range is typical for photodiodes. The photoresponse measured under pulsed illumination is shown in Figure 4e for λ = 1.31 μm, and Figure 4f for λ = 2.2 μm. When the wavelength of the illumination source is λ =1.31 μm, the photocurrent under zero bias is negligible compared to that under a 0.3 V forward bias, with the rise and fall time found to be 74.3 μs and 2.97 ms respectively. These values fall within the range of reported values in the literature for other CQD sensitised phototransistors.[27, 28, 59] However, when the illumination wavelength is λ = 2.2 μm, the photocurrent waveforms show a high signal with 0 V bias, which is heavily suppressed by a 0.3 V forward bias. The rise and fall times are found to be < 20 μs at 0 V bias, limited in this case by our instrumentation. Based on previous studies, the real response speed under this mode of operation is expected to be much faster.[71, 72] These differences in the intensity dependence and response time under different illumination/bias conditions again support our claim that the underlying detection mechanism is switching between that of a phototransistor and a photodiode.

To quantify the performance of the PbS CQD/MoS_2/bP dual-band photodetector, the spectrally dependent responsivity *R*, specific detectivity *D**, and external quantum efficiency η_e are extracted at room temperature. Due to the distinct mechanisms between the photodiode and the phototransistor modes, the *D** is calculated under the two bias conditions using different equations which estimate the fundamental noise current based on the devices' dark behaviour (details

provided in the Experimental Section). The extracted R and D^* of the phototransistor mode under V_{DS} = 0.3 V and λ = 1.31 μm illumination are shown in Figure 5a. R increases as the light power density decreases with a highest value of R = 46 A W^{-1} with a peak D^* of 1.6×10^{11} cm $Hz^{1/2}$ W^{-1}. We note that R can be easily increased in this mode of operation by increasing the V_{DS} (see, for example, larger source-drain biases in Figure 3a), however, in this study we focused on low bias conditions for low power operation. The extracted R and D^* of the photodiode mode under V_{DS} = 0 V and λ = 2.2 μm illumination are also shown in Figure 5b. The value of R remains flat until a power density of ~0.1 W cm^{-2}, whereupon it starts to decrease. The flat region corresponds to an R value of ~0.4 A W^{-1} and a D^* value of $\sim 5 \times 10^9$ cm $Hz^{1/2}$ W^{-1}. These results are included in Table 1, which summaries several representative bias-selectable dual-band photodetectors from the literature. Compared to existing results, the PbS CQD/MoS_2/bP dual-band detector shows excellent performance, particularly the forward bias responsivity. More importantly, its detectivity is the highest among the devices characterised at room temperature. To validate the calculated D^*, noise current density spectra are also experimentally measured (details provided in the Supplementary Section 6). The D^* value extracted with the measured noise current density is similar to the calculated value in the case of the photodiode mode (*i.e.* zero bias conditions). In the case of the phototransistor mode (*i.e.* forward bias conditions), the D^* extracted from the measured noise current is over an order of magnitude lower than the calculated value, likely a consequence of additional noise from the instrumentation with applied bias or other non-fundamental noise mechanisms in the device. The intensity dependent external quantum efficiency is also calculated for both illumination conditions as shown in Figure 5c. A much higher external quantum efficiency is observed for the phototransistor mode which is expected due to its photoconductive gain. Figure 5d shows the spectral responsivity of a representative device under the two modes of operation.

As the response speed of the photodiode mode is < 20 μs (shown in Figure 4f), its photoresponse is not affected by the optical velocity of the interferometer in the FTIR spectrometer. However, the slower fall time when in the photoconductive mode (see Figure 4e) is not fast enough to fully resolve the steady-state photoresponse by the FTIR spectrometer. Therefore, responsivity is characterised under different optical velocities in the FTIR spectrometer, as well under low modulation frequency in a custom-built, near infrared responsivity setup. The *R* values at λ = 1.31μm and 2.2 μm extracted from Figure 5d are also included in Figure 5a and 5b as the red markers, which show reasonable alignment in values between the two characterisation set-ups. Additionally, the spectral photoresponse is examined at both low temperatures and under different back gate bias conditions. These factors are found to result in only minimal improvements in photoresponse, as detailed in the Supplementary Section 7.

Finally, a scanning imaging system is designed to demonstrate the IR imaging capability of the PbS CQD/MoS_2/bP dual-band photodetector. A schematic of the test set-up is presented in Figure 6a, consisting of a blackbody light source which illuminates a transmissive binary mask (patterned with letters “W. BPF” and “W/O. BPF”, shown in Figure 6b), which is imaged onto a device under test (DUT), mounted on a motorised XY stage. Images are collected by scanning a single detector over the image plane in a serpentine pattern. These are taken with and without a bandpass filter (FB2000-500, Thorlabs) in the beam path. With the bandpass filter applied, only light between λ = 1.7 - 2.4 μm is passed (*i.e.* beyond the absorption edge of the PbS CQDs). Figure 6c shows the two normalised illumination spectra—the blackbody source with and without the band pass filter. To demonstrate the performance of the PbS CQD/MoS_2/bP device, a set of images are taken under different bias conditions, each with and without the band pass filter, as shown in Figure 6d-6f. The band pass filter is placed in the beam path for the first half of each scan (corresponding to the

region labelled “W. BPF”), and then removed when the halfway point is reached (corresponding to the region labelled “W/O. BPF”). Figure 6d is taken from the PbS CQD/MoS_2/bP photodetector with a forward bias of V_{DS} = 0.3 V which corresponds to the phototransistor mode of operation. Under these conditions, the detector only resolves features in the bottom half of the pattern. During the top half, no response is obtained as shorter wavelength components are filtered by the bandpass filter. Figure 6e is captured under V_{DS} = 0 V, corresponding to the photodiode mode in which the photoresponse is extended to the MWIR. Consequently, the pattern is fully captured even though the bandpass filter is present on the top half of the pattern. Similarly, Figure 6f which is taken under a reverse bias of V_{DS} = -0.3 V, can also capture the full pattern as the reverse bias is a combination of the two detection modes. These measurements demonstrate that an image acquired under forward bias can serve as a SWIR image. Images taken at zero bias are predominantly sensitive to MWIR illumination, however they are not completely blind to the SWIR signal, leading to some undesired cross-talk (based on Figures 2f and 5d, ~15% of the zero bias photoresponse overlaps with the forward bias photoresponse spectrum). This cross-talk is more pronounced for the reverse bias image. This means that a pure MWIR image would have to be acquired by computationally removing the SWIR component, using information about the relative spectral response in the three modes. Future work could optimise the thickness of the CQD layer, on top of the bP/MoS_2 junction, to serve as a SWIR filter to reduce the cross-talk. In addition, careful tuning of the optical structure (*i.e.* the thickness of the bP, MoS_2 and the substrate oxide) would permit increased absorption in the MWIR and reduced absorption in the SWIR, resulting in reduced optical cross-talk.[71] Regardless, these proof-of-principle results clearly show the potential of the PbS CQD/MoS_2/bP photodetector for spectrally sensitive SWIR/MWIR imaging, which

could be incorporated with the polarisation dependence shown in Figure 3c, to provide further functionality.

Conclusion

In this study we have designed and fabricated mixed-dimensional, bias-selectable PbS CQD/MoS_2/bP dual-band IR photodetectors with excellent performance at room temperature. We demonstrate a hybrid device architecture, which enables switching between photodiode (MWIR) and phototransistor (SWIR) modes of operation by applying a small shift of the source-drain voltage between V_{DS} = 0 V and 0.3 V, respectively. In the photodiode mode, which is sensitive to wavelengths up to $\lambda \approx 4\mu m$, these devices exhibit a room temperature $D^* = 5 \times 10^9$ cm $Hz^{1/2}$ W^{-1} (at λ = 2.2 μm) and a response speed faster than 20 μs. In the photoconductive mode, which is sensitive to wavelengths up to $\lambda \approx 1.45\mu m$, the devices exhibit photoconductive gain allowing a responsivity of up to R = 46 A/W^{-1} and a detectivity of 1.6×10^{11} cm $Hz^{1/2}$ W^{-1} (at λ = 1.31 μm). These devices are also integrated into a scanning imaging set-up, successfully demonstrating that they can be used in spectrally sensitive IR imaging. This study serves as an excellent proof-of-concept for dual-band bias-selectable IR detectors which can switch between detection mechanisms utilising the advantages of both.

Experimental Section

Synthesis of the PbS quantum dots: PbS QDs were synthesized according to the procedure reported by Owen et al.[73] Briefly, Premade lead oleate (Pb-Oleate, 0.3 mmol) and 9.5 ml hexadecane was loaded in a 40 ml vial. This was heated in an oil bath to 120 °C under nitrogen to dissolve the Pb-oleate. Thiourea solution was prepared by heating N-(p-methoxyphenyl)-N'-dodecylthiourea (0.3 mmol) in 0.75 ml of diphenylurea in the same oil bath. A small amount (0.5 ml) of this solution was swiftly injected into the Pb-oleate solution at 120 °C. The reaction was allowed to proceed for 20 mins. After this, the solution was cooled to room temperature. Toluene was added and the solution was loaded into a centrifuge tube. The QD solution was precipitated by adding methyl acetate and centrifuged at 5000 RCF for 5 mins. This cycle was repeated twice more and the precipitate was finally redispersed in toluene and stored in a 3 ml vial in the dark. The size of the nanocrystals was estimated from a reported sizing curve.[67]

Device fabrication: PbS CQD/MoS_2/bP photodetectors were fabricated by first constructing the bP/MoS_2 heterojunction, then coating with the PbS CQDs. To achieve this, high quality bulk bP crystals (from 2Dsemiconductors USA) were exfoliated onto a Si/SiO_2 wafer in an ultraviolet light free, N_2 environment. Similarly, MoS_2 crystals (from 2Dsemiconductors USA) were exfoliated onto a Si/SiO_2 wafer in air. Following exfoliation, the chosen MoS_2 flakes were immediately transferred onto target bP flakes to form heterojunctions via a PMMA based dry transfer process. Subsequently, source and drain regions were defined by electron beam lithography, and Cr (10 nm) / Au (60 nm) contacts were deposited via electron beam evaporation. Following this, PbS CQDs were deposited onto the bP/MoS_2 devices using a layer-by-layer spin-coating process, where 15 μl of oleate ligand capped PbS QD solution (20 mg/ml in toluene) was

drop-cast onto the device chip and spun at 1500 rpm for 1 minute, followed by an identical process with 20 μl 2% 1,2-ethanedithiol (EDT) in acetonitrile to perform a ligand exchange. The above steps were repeated 3 to 5 times to achieve the desired QD thickness.

Absorption spectrum measurements: The absorbance spectrum of dispersed PbS CQDs was collected with a vis-NIR spectrometer (Agilent HP8453). The absorption spectrum of bulk bP was collected using an FTIR microscope (PerkinElmer Frontier) with representative bP flakes being exfoliated onto a quartz substrate for transmission and reflection measurements. The MoS_2 absorbance data was taken from Ref. 66.

Device characterisation: Source-drain current-voltage characteristics of the PbS CQD/MoS_2/bP photodetectors were measured using a Keysight B1500A source measure unit, under dark and illuminated conditions. The light sources for the two illumination test conditions were laser diodes at λ = 1.31 μm (Thorlabs ML725B8F) and at λ = 2.2 μm (CNI MDL-H-2200) respectively. The photocurrent versus illumination intensity measurements were performed under modulated illumination (frequency =120 Hz for λ = 2.2 μm, 10 Hz for λ = 1.31 μm), with accurate photocurrents obtained by amplifying currents using a transimpedance amplifier (Stanford Research Systems SR570) fed into a lock-in amplifier (Stanford Research Systems SR860) triggered by the laser modulation signal. The light intensity was varied using a combination of different laser driving current and neutral density filters placed in the beam path, with its attenuation rate calibrated by a commercial mercury-cadmium-telluride (MCT) photodiode (PVM-10.6, Boston Electronics). The time domain photocurrent waveforms were captured by connecting the amplified modulated photocurrents to an oscilloscope (Tektronix TDS 3034B) with the laser modulation signal as a trigger, from which the device rise/fall times were extracted. Responsivity

values were calculated based on the photocurrent versus illumination intensity measurements. Detectivity values were calculated based on two equations: $D^* = \frac{R\sqrt{A\Delta f}}{i_n}$ for the phototransistor mode and $D^* = \frac{\eta_e \lambda q}{hc}\left(\frac{4kT}{R_0 A}\right)^{-1/2}$ for the photodiode mode,[68, 74] where A is the area of the device, Δf is the frequency bandwidth, i_n is the noise current, λ is the light wavelength, q is the elementary charge, h is the Planck constant, c is the speed of light, k is the Boltzmann constant, T is the temperature and R_0A is the resistance area product. External quantum efficiency was extracted from the responsivity values using $\eta_e = \frac{Rhc}{q\lambda}$.

Spectral characterisation: The spectral photoresponse of the fabricated devices was measured using a commercially available FTIR spectrometer (PerkinElmer Frontier) with a custom-built device test platform positioned at the external detector port. The illumination from a modulated 1200 K blackbody source inside the FTIR, guided to the external port, is aligned to the test platform and focused onto the device under test (DUT). The DUT's signal was then amplified by a transimpedance amplifier (SR570) and fed back into the external signal input port of the FTIR which then performs the Fourier transform to extract a spectrum. The acquired spectrum was corrected using the built-in detector in the FTIR to eliminate the wavelength dependence of the blackbody source. To accurately quantify the responsivity, such as the measurements shown in Figure 5d, the setup was calibrated using a NIST traceable Ge photodiode illuminated under identical conditions. A more detailed explanation of this measurement process is provided elsewhere (see, for example, the Supporting Information of Ref. 46). The photoresponse map of the PbS CQD/MoS_2/bP dual-band detector (see Figure 3a) was obtained by taking the spectral photoresponse measurement at various source-drain biases (from -0.5 V to 0.5 V at a step of 0.1 V). The polarisation dependent photocurrent (Figure 3c and 3d) was measured by placing a wire

grid polariser (WP25M-UB) in the FTIR beam path while recording the device photocurrent at different polarisation angles from 0 to 180° with a step of 10°. The results were corrected for the polarisation dependence of the FTIR source. The dark blue curve in Figure 5d was obtained using a custom built visible to NIR responsivity setup which is limited to wavelengths less than $\lambda = 1.6$ μm. The light path was mechanically chopped at a low frequency (10 Hz) and the modulated signal read by a lock in amplifier (SR510) to capture the full photoresponse while the detector was operating in the phototransistor mode. A NIST traceable Ge photodiode illuminated under identical conditions was used to calibrate this setup.

Laser beam induced current (LBIC): the LBIC mapping was performed on a custom-built 4f-type confocal microscope integrated with a wavelength/intensity tuneable ($\lambda = 1.51 – 1.64$ μm) laser source (Agilent 8164A/81640A) and a fixed wavelength ($\lambda = 1.31$ μm) laser (OZOptics OZ-3000), a galvanometer mirror for scanning the beam and a high speed transimpedance amplifier (Femto DLPCA-200) for amplifying the photocurrent. The laser was scanned over an area while the photocurrent, as well as the reflection signal, was measured and recorded at each pixel. The reflection signal maps, in which the outlines of the metal electrodes were clearly visible, were used to align the LBIC maps to the grey scale microscope image shown in Figure 3b. The spatial x-y resolution for this set-up was approximately 1 μm, estimated by Abbe's diffraction formula. Scan step sizes of 0.25 μm (for $V_{DS} = 0$ V) and 1 μm (for $V_{DS} = 0.3$ V) were used for the measurements.

Scanning imaging: The imaging in Figure 6 was performed by scanning the photodetector across the image plane to construct a complete image of the transmissive object. To achieve this, the photodetector was mounted onto a three-axis motor-controlled stage (Thorlabs DRV014) which was programmed to scan the image plane in a serpentine pattern with a step size of 10 μm.

The transmissive pattern to be imaged (non-transmissive area defined by an opaque Au layer) was illuminated from the rear using a broadband light source (Thorlabs SLS 203L). Light passing through the transmissive pattern was modulated by a chopper and directed into a 10× reflective objective, after which it was focused on the device under test. A filter holder was placed in the light path to allow the addition/removal of a bandpass filter (FB2000-500, Thorlabs) to create different illumination spectra. The photocurrents obtained from the device under test were amplified by a transimpedance amplifier (Stanford Research Systems SR570) and measured using a lock-in amplifier (Stanford Research Systems SR860). The variation of the light source intensity across the image plane was corrected using an image taken without the transmissive object.

Acknowledgements

This work was performed in part at the Melbourne Center for Nanofabrication (MCN) and the Melbourne Characterisation and Fabrication Platform (MCFP). This work was supported by the Australian Research Council (DE210101129). J.B. acknowledges support from the MCN technology fellowship program. P.M. and A.A. thank the ARC for support through Grant CE170100026. A.P. acknowledges the ARC Centre of Excellence for Quantum Computation and Communication Technology (CE170100012).

Supporting Information Available:

Illustrative energy band diagrams of the PbS CQD/MoS_2/bP dual-band photodetector in the two operation modes; spectral response of MoS_2 phototransistors with PbS and PbSe CQDs; optical microscope image and characterisation of three-terminal devices; device current-voltage sweep

changes before and after depositing CQDs; simple device modelling; noise current spectral density measurement; temperature-, gate- and time-dependent spectral photoresponse.

References

(1) Rogalski, A. Recent Progress in Infrared Detector Technologies. *Infrared Phys. Technol.* **2011**, *54*, 136-154.

(2) Abedin, M. N.; Tamer, F. R.; Ishwara, B. B.; Yegao, X.; Sumith, V. B.; Sarath, D. G. Progress of Multicolor Single Detector to Detector Array Development for Remote Sensing. In *Infrared Spaceborne Remote Sensing XII*, Proceedings of SPIE Optical Science and Technology, Denver, 4 November; **2004**; Vol. 5543, pp 239-247.

(3) Bullock, J.; Amani, M.; Cho, J.; Chen, Y.-Z.; Ahn, G. H.; Adinolfi, V.; Shrestha, V. R.; Gao, Y.; Crozier, K. B.; Chueh, Y.-L.; et al. Polarization-Resolved Black Phosphorus/Molybdenum Disulfide Mid-Wave Infrared Photodiodes with High Detectivity at Room Temperature. *Nat. Photonics* **2018**, *12*, 601-607.

(4) Wu, D.; Guo, J.; Du, J.; Xia, C.; Zeng, L.; Tian, Y.; Shi, Z.; Tian, Y.; Li, X. J.; Tsang, Y. H.; et al. Highly Polarization-Sensitive, Broadband, Self-Powered Photodetector Based on Graphene/PdSe2/Germanium Heterojunction. *ACS Nano* **2019**, *13*, 9907-9917.

(5) Wang, Y.; Wu, P.; Wang, Z.; Luo, M.; Zhong, F.; Ge, X.; Zhang, K.; Peng, M.; Ye, Y.; Li, Q.; et al. Air-Stable Low-Symmetry Narrow-Bandgap 2D Sulfide Niobium for Polarization Photodetection. *Adv. Mater.* **2020**, *32*, 2005037.

(6) Lockwood, A. H.; Balon, J. R.; Chia, P. S.; Renda, F. J. Two-Color Detector Arrays by PbTe/Pb0.8Sn0.2Te Liquid Phase Epitaxy. *Infrared Phys.* **1976**, *16*, 509-514.

(7) Rajavel, R. D.; Jamba, D. M.; Jensen, J. E.; Wu, O. K.; Brewer, P. D.; Wilson, J. A.; Johnson, J. L.; Patten, E. A.; Kosai, K.; Caulfield, J. T.; et al. Molecular Beam Epitaxial Growth and Performance of HgCdTe-Based Simultaneous-Mode Two-Color Detectors. *J. Electron. Mater.* **1998**, *27*, 747-751.

(8) Hoang, A. M.; Chen, G.; Haddadi, A.; Razeghi, M. Demonstration of High Performance Bias-Selectable Dual-Band Short-/Mid-Wavelength Infrared Photodetectors Based on Type-II InAs/GaSb/AlSb Superlattices. *Appl. Phys. Lett.* **2013**, *102*, 011108.

(9) Gautam, N.; Naydenkov, M.; Myers, S.; Barve, A. V.; Plis, E.; Rotter, T.; Dawson, L. R.; Krishna, S. Three Color Infrared Detector Using InAs/GaSb Superlattices with Unipolar Barriers. *Appl. Phys. Lett.* **2011**, *98*, 121106.

(10) Hipwood, L. G.; Jones, C. L.; Maxey, C. D.; Lau, H. W.; Fitzmaurice, J.; Catchpole, R. A.; Ordish, M. Three-Color MOVPE MCT Diodes. In *Infrared Technology and Applications XXXII*, Proceedings of SPIE Defense and Security Symposium, 17 May; **2006**; Vol. 6206, p 620612.

(11) Rogalski, A.; Antoszewski, J.; Faraone, L. Third-Generation Infrared Photodetector Arrays. *J. Appl. Phys.* **2009**, *105*, 091101.

(12) Downs, C.; Vandervelde, T. E. Progress in Infrared Photodetectors Since 2000. *Sensors*, **2013**; Vol. 13, pp 5054-5098.

(13) Levine, B. F. Quantum‐Well Infrared Photodetectors. *J. Appl. Phys.* **1993**, *74*, R1-R81.

(14) Wu, W.; Bonakdar, A.; Mohseni, H. Plasmonic Enhanced Quantum Well Infrared Photodetector with High Detectivity. *Appl. Phys. Lett.* **2010**, *96*, 161107.

(15) Ting, D. Z. Y.; Soibel, A.; Höglund, L.; Nguyen, J.; Hill, C. J.; Khoshakhlagh, A.; Gunapala, S. D. Type-II Superlattice Infrared Detectors. In *Semiconductors and Semimetals*; Vol. 84; Elsevier, **2011**.

(16) Alshahrani, D. O.; Kesaria, M.; Anyebe, E. A.; Srivastava, V.; Huffaker, D. L. Emerging Type-II Superlattices of InAs/InAsSb and InAs/GaSb for Mid-Wavelength Infrared Photodetectors. *Adv. Photonics Res.* **2022**, *3*, 2100094.

(17) Martyniuk, P.; Rogalski, A. Quantum-Dot Infrared Photodetectors: Status and Outlook. *Prog. Quantum Electron.* **2008**, *32*, 89-120.

(18) Liu, H. C.; Gao, M.; McCaffrey, J.; Wasilewski, Z. R.; Fafard, S. Quantum Dot Infrared Photodetectors. *Appl. Phys. Lett.* **2000**, *78*, 79-81.

(19) Livache, C.; Martinez, B.; Goubet, N.; Gréboval, C.; Qu, J.; Chu, A.; Royer, S.; Ithurria, S.; Silly, M. G.; Dubertret, B.; et al. A Colloidal Quantum Dot Infrared Photodetector and Its Use for Intraband Detection. *Nat. Commun.* **2019**, *10*, 2125.
(20) Long, M.; Wang, P.; Fang, H.; Hu, W. Progress, Challenges, and Opportunities for 2D Material Based Photodetectors. *Adv. Funct. Mater.* **2019**, *29*, 1803807.
(21) Adinolfi, V.; Sargent, E. H. Photovoltage Field-Effect Transistors. *Nature* **2017**, *542*, 324-327.
(22) Goossens, S.; Navickaite, G.; Monasterio, C.; Gupta, S.; Piqueras, J. J.; Pérez, R.; Burwell, G.; Nikitskiy, I.; Lasanta, T.; Galán, T.; et al. Broadband Image Sensor Array Based on Graphene–CMOS Integration. *Nat. Photonics* **2017**, *11*, 366-371.
(23) Sukhovatkin, V.; Hinds, S.; Brzozowski, L.; Sargent, E. H. Colloidal Quantum-Dot Photodetectors Exploiting Multiexciton Generation. *Science* **2009**, *324*, 1542-1544.
(24) Clifford, J. P.; Konstantatos, G.; Johnston, K. W.; Hoogland, S.; Levina, L.; Sargent, E. H. Fast, Sensitive and Spectrally Tuneable Colloidal-Quantum-Dot Photodetectors. *Nat. Nanotechnol.* **2009**, *4*, 40-44.
(25) Melnychuk, C.; Guyot-Sionnest, P. Slow Auger Relaxation in HgTe Colloidal Quantum Dots. *J. Phys. Chem. Lett.* **2018**, *9*, 2208-2211.
(26) Rogalski, A. HgCdTe Infrared Detector Material: History, Status and Outlook. *Rep. Prog. Phys.* **2005**, *68*, 2267.
(27) Kufer, D.; Nikitskiy, I.; Lasanta, T.; Navickaite, G.; Koppens, F. H. L.; Konstantatos, G. Hybrid 2D–0D MoS2–PbS Quantum Dot Photodetectors. *Adv. Mater.* **2015**, *27*, 176-180.
(28) Sun, Z.; Liu, Z.; Li, J.; Tai, G.-a.; Lau, S.-P.; Yan, F. Infrared Photodetectors Based on CVD-Grown Graphene and PbS Quantum Dots with Ultrahigh Responsivity. *Adv. Mater.* **2012**, *24*, 5878-5883.
(29) Pejović, V.; Georgitzikis, E.; Lieberman, I.; Malinowski, P. E.; Heremans, P.; Cheyns, D. Photodetectors Based on Lead Sulfide Quantum Dot and Organic Absorbers for Multispectral Sensing in the Visible to Short-Wave Infrared Range. *Adv. Funct. Mater.* **2022**, *32*, 2201424.
(30) Xu, K.; Xiao, X.; Zhou, W.; Jiang, X.; Wei, Q.; Chen, H.; Deng, Z.; Huang, J.; Chen, B.; Ning, Z. Inverted Si:PbS Colloidal Quantum Dot Heterojunction-Based Infrared Photodetector. *ACS Appl. Mater. Interfaces* **2020**, *12*, 15414-15421.
(31) Kundu, B.; Özdemir, O.; Dalmases, M.; Kumar, G.; Konstantatos, G. Hybrid 2D-0D MoS2–PbSe Quantum Dot Broadband Photodetectors with High-Sensitivity and Room-Temperature Operation at 2.5 µm. *Adv. Opt. Mater.* **2021**, *9*, 2101378.
(32) Qu, J.; Goubet, N.; Livache, C.; Martinez, B.; Amelot, D.; Gréboval, C.; Chu, A.; Ramade, J.; Cruguel, H.; Ithurria, S.; et al. Intraband Mid-Infrared Transitions in Ag2Se Nanocrystals: Potential and Limitations for Hg-Free Low-Cost Photodetection. *J. Phys. Chem. C* **2018**, *122*, 18161-18167.
(33) Chen, M.; Hao, Q.; Luo, Y.; Tang, X. Mid-Infrared Intraband Photodetector Via High Carrier Mobility HgSe Colloidal Quantum Dots. *ACS Nano* **2022**, *16*, 11027-11035.
(34) Shen, G.; Guyot-Sionnest, P. HgS and HgS/CdS Colloidal Quantum Dots with Infrared Intraband Transitions and Emergence of a Surface Plasmon. *J. Phys. Chem. C* **2016**, *120*, 11744-11753.
(35) Huo, N.; Gupta, S.; Konstantatos, G. MoS2–HgTe Quantum Dot Hybrid Photodetectors Beyond 2 µm. *Adv. Mater.* **2017**, *29*, 1606576.
(36) Tang, X.; Ackerman, M. M.; Chen, M.; Guyot-Sionnest, P. Dual-Band Infrared Imaging Using Stacked Colloidal Quantum Dot Photodiodes. *Nat. Photonics* **2019**, *13*, 277-282.
(37) SWIR Vision Systems (*CQD Sensor Technology)*. **2023**. https://www.swirvisionsystems.com/cqd-sensor-technology/ (accessed 2023 01.24).
(38) Xia, F.; Wang, H.; Xiao, D.; Dubey, M.; Ramasubramaniam, A. Two-Dimensional Material Nanophotonics. *Nat. Photonics* **2014**, *8*, 899-907.
(39) Zhang, B. Y.; Liu, T.; Meng, B.; Li, X.; Liang, G.; Hu, X.; Wang, Q. J. Broadband High Photoresponse from Pure Monolayer Graphene Photodetector. *Nat. Commun.* **2013**, *4*, 1811.

(40) Liu, C.-H.; Chang, Y.-C.; Norris, T. B.; Zhong, Z. Graphene Photodetectors with Ultra-Broadband and High Responsivity at Room Temperature. *Nat. Nanotechnol.* **2014**, *9*, 273-278.
(41) Amani, M.; Tan, C.; Zhang, G.; Zhao, C.; Bullock, J.; Song, X.; Kim, H.; Shrestha, V. R.; Gao, Y.; Crozier, K. B.; et al. Solution-Synthesized High-Mobility Tellurium Nanoflakes for Short-Wave Infrared Photodetectors. *ACS Nano* **2018**, *12*, 7253-7263.
(42) Liu, J.; Hao, Q.; Gan, H.; Li, P.; Li, B.; Tu, Y.; Zhu, J.; Qi, D.; Chai, Y.; Zhang, W.; et al. Selectively Modulated Photoresponse in Type-I Heterojunction for Ultrasensitive Self-Powered Photodetectors. *Laser Photonics Rev.* **2022**, *16*, 2200338.
(43) Tong, L.; Huang, X.; Wang, P.; Ye, L.; Peng, M.; An, L.; Sun, Q.; Zhang, Y.; Yang, G.; Li, Z.; et al. Stable Mid-Infrared Polarization Imaging Based on Quasi-2D Tellurium at Room Temperature. *Nat. Commun.* **2020**, *11*, 2308.
(44) Huang, H.; Wang, J.; Hu, W.; Liao, L.; Wang, P.; Wang, X.; Gong, F.; Chen, Y.; Wu, G.; Luo, W.; et al. Highly Sensitive Visible to Infrared MoTe2 Photodetectors Enhanced by the Photogating Effect. *Nanotechnology* **2016**, *27*, 445201.
(45) Chen, Y.; Wang, X.; Wu, G.; Wang, Z.; Fang, H.; Lin, T.; Sun, S.; Shen, H.; Hu, W.; Wang, J.; et al. High-Performance Photovoltaic Detector Based on MoTe2/MoS2 Van Der Waals Heterostructure. *Small* **2018**, *14*, 1703293.
(46) Yan, W.; Johnson, B. C.; Balendhran, S.; Cadusch, J.; Yan, D.; Michel, J. I.; Wang, S.; Zheng, T.; Crozier, K.; Bullock, J. Visible to Short-Wave Infrared Photodetectors Based on ZrGeTe4 Van Der Waals Materials. *ACS Appl. Mater. Interfaces* **2021**, *13*, 45881-45889.
(47) Bai, R.; Xiong, T.; Zhou, J.; Liu, Y.-Y.; Shen, W.; Hu, C.; Yan, F.; Wang, K.; Wei, D.; Li, J.; et al. Polarization-Sensitive and Wide-Spectrum Photovoltaic Detector Based on Quasi-1D ZrGeTe4 Nanoribbon. *InfoMat* **2022**, *4*, e12258.
(48) Amani, M.; Regan, E.; Bullock, J.; Ahn, G. H.; Javey, A. Mid-Wave Infrared Photoconductors Based on Black Phosphorus-Arsenic Alloys. *ACS Nano* **2017**, *11*, 11724-11731.
(49) Long, M.; Gao, A.; Wang, P.; Xia, H.; Ott, C.; Pan, C.; Fu, Y.; Liu, E.; Chen, X.; Lu, W.; et al. Room Temperature High-Detectivity Mid-Infrared Photodetectors Based on Black Arsenic Phosphorus. *Sci. Adv.* **2017**, *3*, e1700589.
(50) Zhao, C.; Tan, C.; Lien, D.-H.; Song, X.; Amani, M.; Hettick, M.; Nyein, H. Y. Y.; Yuan, Z.; Li, L.; Scott, M. C.; et al. Evaporated Tellurium Thin Films for P-Type Field-Effect Transistors and Circuits. *Nat. Nanotechnol.* **2020**, *15*, 53-58.
(51) Hwangbo, S.; Hu, L.; Hoang, A. T.; Choi, J. Y.; Ahn, J.-H. Wafer-Scale Monolithic Integration of Full-Colour Micro-Led Display Using MoS2 Transistor. *Nat. Nanotechnol.* **2022**.
(52) Youngblood, N.; Chen, C.; Koester, S. J.; Li, M. Waveguide-Integrated Black Phosphorus Photodetector with High Responsivity and Low Dark Current. *Nat. Photonics* **2015**, *9*, 247-252.
(53) Yuan, S.; Naveh, D.; Watanabe, K.; Taniguchi, T.; Xia, F. A Wavelength-Scale Black Phosphorus Spectrometer. *Nat. Photonics* **2021**, *15*, 601-607.
(54) Kim, H.; Uddin, S. Z.; Lien, D.-H.; Yeh, M.; Azar, N. S.; Balendhran, S.; Kim, T.; Gupta, N.; Rho, Y.; Grigoropoulos, C. P.; et al. Actively Variable-Spectrum Optoelectronics with Black Phosphorus. *Nature* **2021**, *596*, 232-237.
(55) Chen, C.; Youngblood, N.; Peng, R.; Yoo, D.; Mohr, D. A.; Johnson, T. W.; Oh, S.-H.; Li, M. Three-Dimensional Integration of Black Phosphorus Photodetector with Silicon Photonics and Nanoplasmonics. *Nano Lett.* **2017**, *17*, 985-991.
(56) Yuan, H.; Liu, X.; Afshinmanesh, F.; Li, W.; Xu, G.; Sun, J.; Lian, B.; Curto, A. G.; Ye, G.; Hikita, Y.; et al. Polarization-Sensitive Broadband Photodetector Using a Black Phosphorus Vertical P–N Junction. *Nat. Nanotechnol.* **2015**, *10*, 707-713.
(57) Yang, J.; Xu, R.; Pei, J.; Myint, Y. W.; Wang, F.; Wang, Z.; Zhang, S.; Yu, Z.; Lu, Y. Optical Tuning of Exciton and Trion Emissions in Monolayer Phosphorene. *Light Sci. Appl.* **2015**, *4*, e312-e312.

(58) Das, S.; Zhang, W.; Demarteau, M.; Hoffmann, A.; Dubey, M.; Roelofs, A. Tunable Transport Gap in Phosphorene. *Nano Lett.* **2014**, *14*, 5733-5739.
(59) Konstantatos, G.; Badioli, M.; Gaudreau, L.; Osmond, J.; Bernechea, M.; de Arquer, F. P. G.; Gatti, F.; Koppens, F. H. L. Hybrid Graphene–Quantum Dot Phototransistors with Ultrahigh Gain. *Nat. Nanotechnol.* **2012**, *7*, 363-368.
(60) Wu, P.; Ye, L.; Tong, L.; Wang, P.; Wang, Y.; Wang, H.; Ge, H.; Wang, Z.; Gu, Y.; Zhang, K.; et al. Van Der Waals Two-Color Infrared Photodetector. *Light Sci. Appl.* **2022**, *11*, 6.
(61) Chang, T.-Y.; Chen, P.-L.; Chen, P.-S.; Li, W.-Q.; Li, J.-X.; He, M.-Y.; Chao, J.-T.; Ho, C.-H.; Liu, C.-H. Van Der Waals Heterostructure Photodetectors with Bias-Selectable Infrared Photoresponses. *ACS Appl. Mater. Interfaces* **2022**, *14*, 32665-32674.
(62) Jiang, W.; Zheng, T.; Wu, B.; Jiao, H.; Wang, X.; Chen, Y.; Zhang, X.; Peng, M.; Wang, H.; Lin, T.; et al. A Versatile Photodetector Assisted by Photovoltaic and Bolometric Effects. *Light Sci. Appl.* **2020**, *9*, 160.
(63) Luo, H.; Wang, B.; Wang, E.; Wang, X.; Sun, Y.; Li, Q.; Fan, S.; Cheng, C.; Liu, K. Phase-Transition Modulated, High-Performance Dual-Mode Photodetectors Based on WSe2/VO2 Heterojunctions. *Appl. Phys. Rev.* **2019**, *6*, 041407.
(64) Du, M.; Cui, X.; Yoon, H. H.; Das, S.; Uddin, M. D. G.; Du, L.; Li, D.; Sun, Z. Switchable Photoresponse Mechanisms Implemented in Single Van Der Waals Semiconductor/Metal Heterostructure. *ACS Nano* **2022**, *16*, 568-576.
(65) Liu, J.; Liu, P.; Chen, D.; Shi, T.; Qu, X.; Chen, L.; Wu, T.; Ke, J.; Xiong, K.; Li, M.; et al. A near-Infrared Colloidal Quantum Dot Imager with Monolithically Integrated Readout Circuitry. *Nat. Electron.* **2022**, *5*, 443-451.
(66) Song, B.; Gu, H.; Fang, M.; Chen, X.; Jiang, H.; Wang, R.; Zhai, T.; Ho, Y.-T.; Liu, S. Layer-Dependent Dielectric Function of Wafer-Scale 2D MoS2. *Adv. Opt. Mater.* **2019**, *7*, 1801250.
(67) Moreels, I.; Lambert, K.; Smeets, D.; De Muynck, D.; Nollet, T.; Martins, J. C.; Vanhaecke, F.; Vantomme, A.; Delerue, C.; Allan, G.; et al. Size-Dependent Optical Properties of Colloidal PbS Quantum Dots. *ACS Nano* **2009**, *3*, 3023-3030.
(68) Rogalski, A.; Martyniuk, P.; Kopytko, M.; Hu, W. Trends in Performance Limits of the Hot Infrared Photodetectors. *Appl. Sci.* **2021**, *11*.
(69) Huang, L.; Dong, B.; Guo, X.; Chang, Y.; Chen, N.; Huang, X.; Liao, W.; Zhu, C.; Wang, H.; Lee, C.; et al. Waveguide-Integrated Black Phosphorus Photodetector for Mid-Infrared Applications. *ACS Nano* **2019**, *13*, 913-921.
(70) Fang, H.; Hu, W. Photogating in Low Dimensional Photodetectors. *Adv. Sci.* **2017**, *4*, 1700323.
(71) Yan, W.; Shresha, V. R.; Jeangros, Q.; Azar, N. S.; Balendhran, S.; Ballif, C.; Crozier, K.; Bullock, J. Spectrally Selective Mid-Wave Infrared Detection Using Fabry-Pérot Cavity Enhanced Black Phosphorus 2D Photodiodes. *ACS Nano* **2020**, *14*, 13645-13651.
(72) Chen, P.-L.; Chen, Y.; Chang, T.-Y.; Li, W.-Q.; Li, J.-X.; Lee, S.; Fang, Z.; Li, M.; Majumdar, A.; Liu, C.-H. Waveguide-Integrated Van Der Waals Heterostructure Mid-Infrared Photodetector with High Performance. *ACS Appl. Mater. Interfaces* **2022**, *14*, 24856-24863.
(73) Hendricks, M. P.; Campos, M. P.; Cleveland, G. T.; Jen-La Plante, I.; Owen, J. S. A Tunable Library of Substituted Thiourea Precursors to Metal Sulfide Nanocrystals. *Science* **2015**, *348*, 1226-1230.
(74) Piotrowski, J.; Gawron, W. Ultimate Performance of Infrared Photodetectors and Figure of Merit of Detector Material. *Infrared Phys. Technol.* **1997**, *38*, 63-68.
(75) Razeghi, M.; Haddadi, A.; Dehzangi, A.; Chevallier, R.; Yang, T. Recent Advances in InAs/InAs1-xSbx/AlAs1-xSbx Gap-Engineered Type-II Superlattice-Based Photodetectors. In *Infrared Technology and Applications XLIII*, Proceedings of SPIE Defense + Security, Anaheim, 9 May; **2017**; Vol. 10177, p 1017705.
(76) Jiang, Z.; Han, X.; Sun, Y.-Y.; Guo, C.-Y.; Lv, Y.-X.; Hao, H.-Y.; Jiang, D.-W.; Wang, G.-W.; Xu, Y.-Q.; Niu, Z.-C. Bias-Selectable Mid-/Long-Wave Dual Band Infrared Focal Plane Array Based on Type-II InAs/GaSb Superlattice. *Infrared Phys. Technol.* **2017**, *86*, 159-164.

(77) Gunapala, S. D.; Bandara, S. V.; Liu, J. K.; Mumolo, J. M.; Ting, D. Z.; Hill, C. J.; Nguyen, J.; Simolon, B.; Woolaway, J.; Wang, S. C.; et al. Demonstration of Megapixel Dual-Band QWIP Focal Plane Array. *IEEE J. Quantum Electron.* **2010**, *46*, 285-293.
(78) Wilson, J. A.; Patten, E. A.; Chapman, G. R.; Kim, K.; Baumgratz, B.; Goetz, P.; Tighe, S. J.; Risser, R. F.; Herald, R. F.; William, A. R.; et al. Integrated Two-Color Detection for Advanced Focal Plane Array (FPA) Applications. In *Infrared Detectors: State of the Art II*, Proceedings of SPIE-International Symposium on Optics, Imaging, and Instrumentation, San Diego, 7 October; **1994**; Vol. 2274, pp 117-125.
(79) Talamas Simola, E.; Kiyek, V.; Ballabio, A.; Schlykow, V.; Frigerio, J.; Zucchetti, C.; De Iacovo, A.; Colace, L.; Yamamoto, Y.; Capellini, G.; et al. CMOS-Compatible Bias-Tunable Dual-Band Detector Based on GeSn/Ge/Si Coupled Photodiodes. *ACS Photonics* **2021**, *8*, 2166-2173.

Table 1. Compilation of representative bias-selectable dual-band IR photodetectors from the literature. The first section of the table contains results for conventional materials, the second section contains results for low-dimensional materials.

Device	Detail	Cut-off wavelength	Temp.	Responsivity (A W^{-1})	D* (cm $Hz^{1/2}$ W^{-1})	R/F time	Bias (V)	Ref.
$InAs/InAs_{1-x}Sb_x$	T2SL	~4.3 μm ~9.5 μm	77 K 77 K	1.5 2.25	8.2×10^{12} 1.6×10^{11}	N/A N/A	0.1 -0.15	75
InAs/GaSb	T2SL	~4.5 μm ~10 μm	77 K 77 K	N/A N/A	2.1×10^{12} 2.3×10^{10}	N/A N/A	0 -0.17	76
AlGaAs/GaAs	QWIP*	~5.1 μm ~8.8 μm	90 K 70 K	N/A ~0.15	4×10^{11} 1×10^{11}	N/A N/A	-1 -1	77
HgCdTe	b2b diode	~5 μm ~9.4 μm	80 K 80 K	80% (EQE) 61% (EQE)	N/A N/A	N/A N/A	0 0.2	78
Si/Ge/GeSn	Epitaxial bulk	~1.6 μm ~2.4 μm	RT RT	0.41 0.64	1.9×10^{10} 4×10^{9}	N/A N/A	0.3 -0.3	79
$HgTe/Ag_2Te$ /HgTe	QD b2b diode	~2.5 μm ~5 μm	85 K 85 K	0.4 N/A	1×10^{11} 3×10^{10}	<2.5 μs <2.5 μs	0.5 -0.3	36
$bP/MoS_2/Si$	Mixed-D b2b diode	~0.9 μm ~3.9 μm	RT RT	N/A 0.25	9.8×10^{8} 6.4×10^{9}	50 μs 20 μs	N/A N/A	60
$bP/MoS_2/MoTe_2$	2D b2b diode	~1.4 μm ~4 μm	RT RT	0.38 0.38	N/A N/A	37 ns 41 ns	0.5 -0.5	61
This work $PbS/MoS_2/bP$	Mixed-dim	~1.5 μm ~4 μm	RT RT	46 0.4	1.6×10^{11} 5×10^{9}	3 ms < 20 μs	0.3 0	This work

R/F time = rise and fall time; T2SL = type 2 superlattice; QWIP = quantum well infrared photodetector; b2b = back-to-back diode; mixed-dim = mixed dimensional; RT = room temperature. *Note that the QWIP device is a dual-band photodetector with 2 isolated devices rather than bias-selectable.

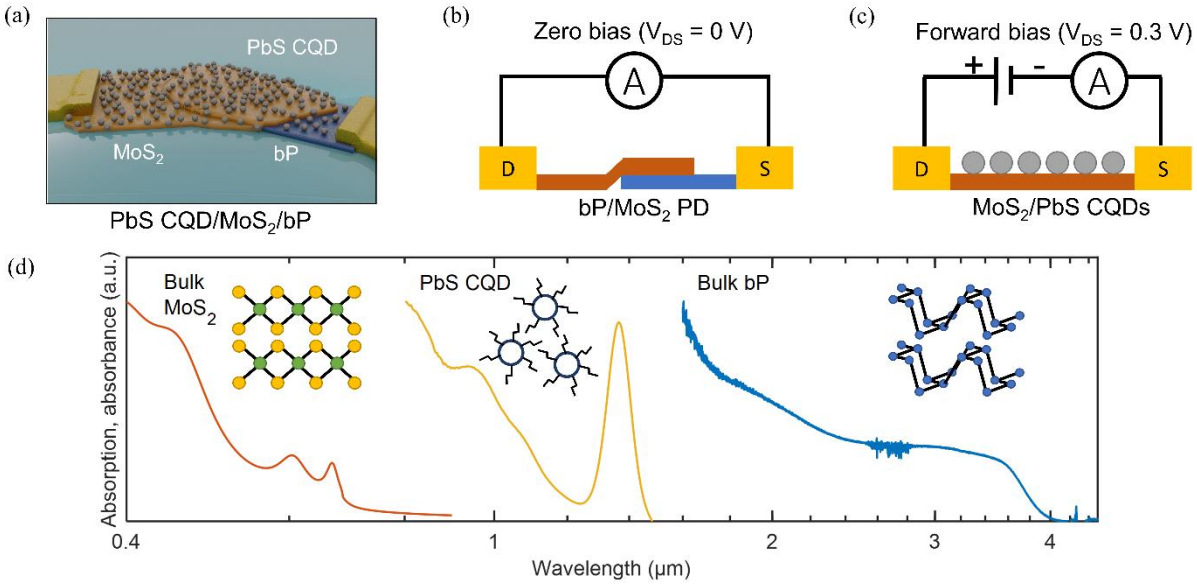

Figure 1. (a) Conceptual schematic of the PbS CQD /MoS_2/bP dual-band bias-selectable detector capable of altering its spectral photoresponse under different bias conditions. The two cross sections in (b) and (c) show the hypothetical active device region under zero and forward bias, respectively. (d) Absorption spectrum of bulk bP, absorbance spectra of bulk MoS_2 (data acquired from Ref. 59) as well as a PbS CQD solution.

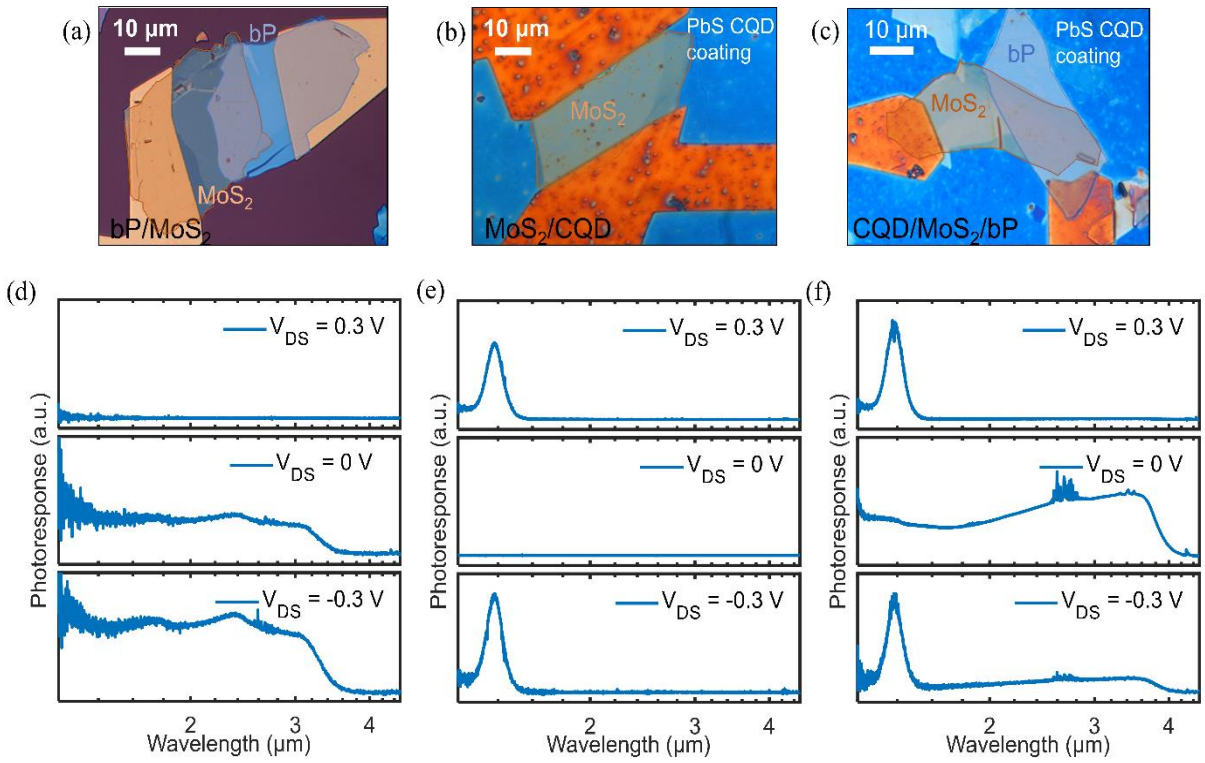

Figure 2. Optical microscope images of representative devices: (a) bP/MoS_2 photodiode; (b) PbS CQD/MoS_2 phototransistor; and (c) PbS CQD/MoS_2/bP dual band photodetector. The continuous PbS CQD film can be clearly seen by comparing the background of (a) to (b) or (c). Micron scale particles in (b) and (c) are CQD aggregates. (d) PbS CQD/MoS_2 phototransistor spectral response under positive (top), zero (middle) and negative (bottom) source-drain bias. (e) bP/MoS_2 photodiode spectral response under positive (top), zero (middle) and negative (bottom) source-drain bias. (f) PbS CQD/MoS_2/bP photodetector spectral response under positive (top), zero (middle) and negative (bottom) source-drain bias. The y axes of (d), (e) and (f) are of a linear scale. All devices are measured at room temperature under V_{GS} = 0 V. Note that the relative magnitude of the PbS CQD response in these plots is curtailed as its response speed is not sufficient to be fully captured by the optical velocity of the FTIR. Also note that the noise occurring around λ = 2.75 μm is due to atmospheric absorption from CO_2/H_2O.

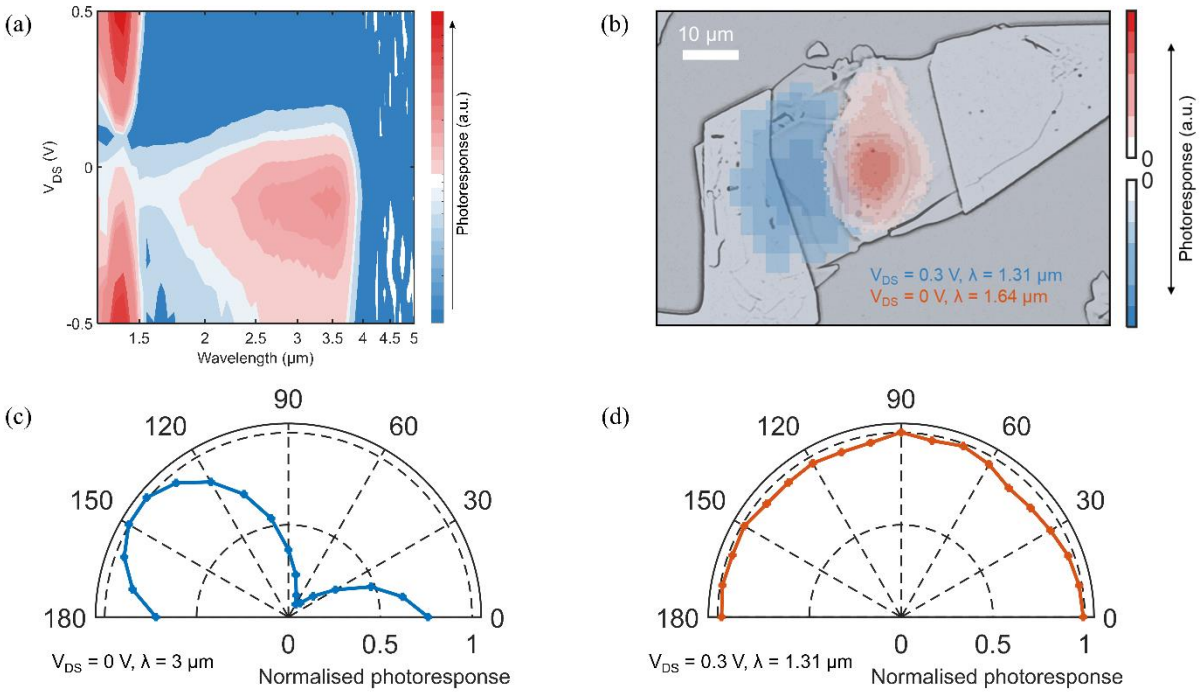

Figure 3. (a) Photoresponse of the PbS CQD /MoS_2/bP dual-band detector with respect to the wavelength of the illumination source, and source-drain bias voltage. (b) Two laser-beam induced current (LBIC) maps taken of a representative PbS CQD/MoS_2/bP dual-band detector under two test conditions: *i.* V_{DS} = 0.3 V, λ = 1.31 μm (blue); and *ii.* V_{DS} = 0 V, λ = 1.64 μm (red). The grey scale microscope image in the background is used to show the approximate regions of detection under the two conditions. Linear polarisation dependent normalised photocurrent of the detector under (c) zero source-drain bias (V_{DS} = 0 V, at λ = 3 μm), (d) positive source-drain bias (V_{DS} = 0.3 V, at λ = 1.31 μm).

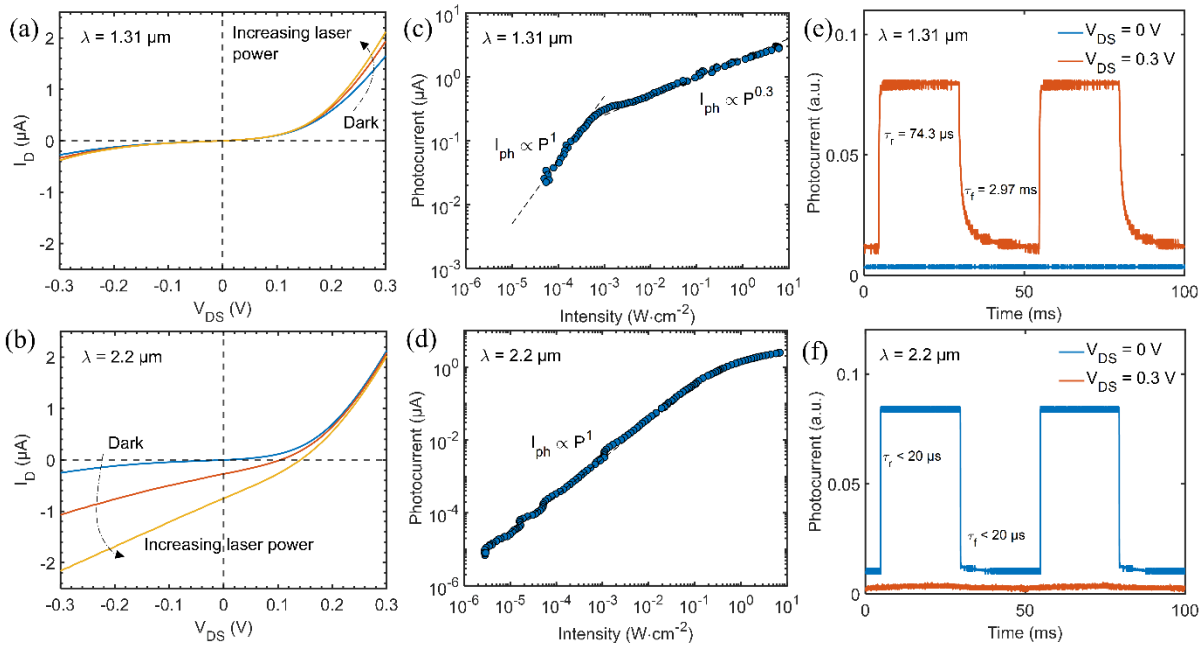

Figure 4. Source-drain current-voltage characteristics of a representative PbS CQD/MoS_2/bP photodetector under dark and increasing illumination intensity: (a) λ = 1.31 μm, (b) λ = 2.2 μm. Linearity of photoresponse with incident intensity from a representative PbS CQD/MoS_2/bP photodetector under (c) λ = 1.31 μm at V_{DS} = 0.3 V; and (d) λ = 2.2 μm at V_{DS} = 0 V. Pulsed photoresponse of a representative PbS CQD/MoS_2/bP photodetector under positive (V_{DS} = 0.3 V) and zero bias (V_{DS} = 0 V), illuminated with modulated light at a fixed intensity (e) λ = 1.31 μm and (f) λ = 2.2 μm. Data has been shifted vertically without scaling for clarity. Rise and fall times are calculated between 10%-90% of the peak response. All devices were measured at room temperature under V_{GS} = 0 V.

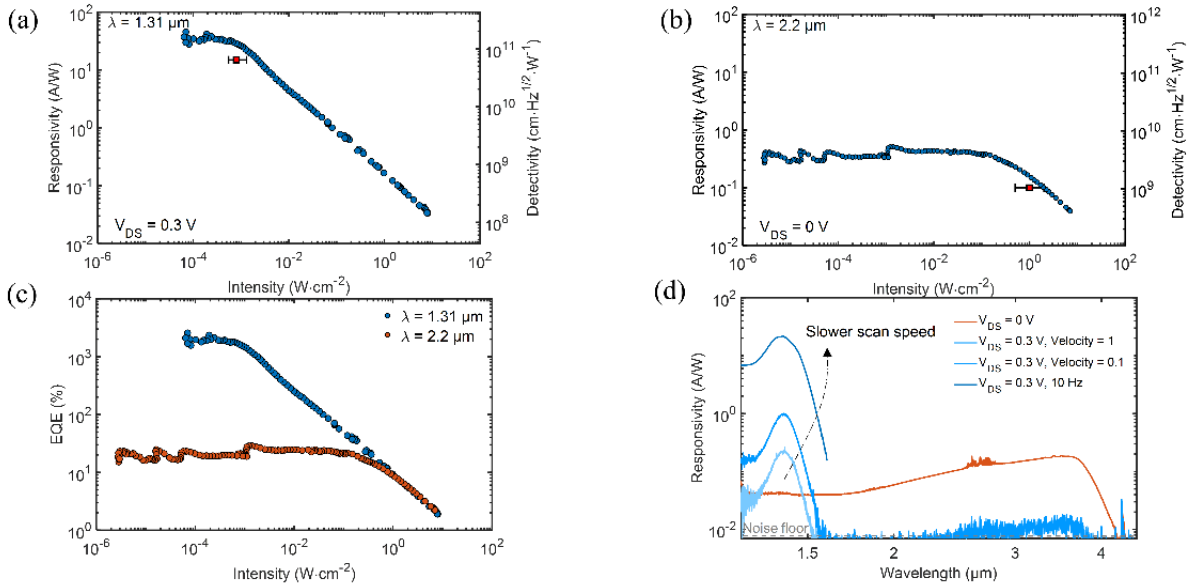

Figure 5. (a) Responsivity (left y-axis) and specific detectivity (right y-axis) of the representative PbS CQD/MoS_2/bP photodetector as a function of illumination intensity under (a) λ = 1.31 μm at V_{DS} = 0.3 V; and (b) λ = 2.2 μm at V_{DS} = 0 V. (c) External quantum efficiency of the representative PbS CQD/MoS_2/bP photodetector under the conditions in (a) and (b). (d) Wavelength-dependent responsivity of the device under positive (V_{DS} = 0.3 V) and zero bias (V_{DS} = 0 V). All devices were measured at room temperature under V_{GS} = 0 V.

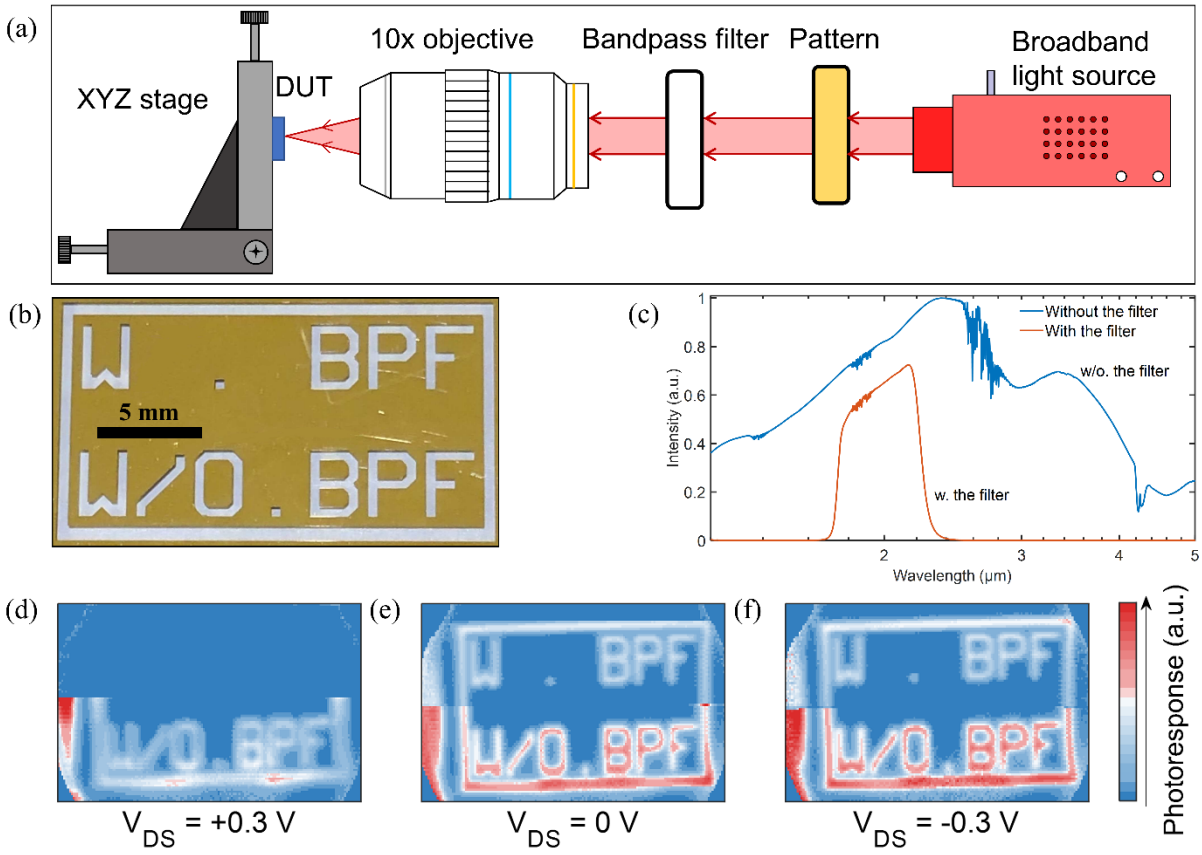

Figure 6. (a) Schematic showing the integration of the dual-band bias-selectable PbS CQD/MoS_2/bP photodetector with a scanning imaging set-up. (b) Photograph of the binary mask patterned on a glass slide with Au. (c) Nomalised spectral density of the broad-spectrum infrared illumination source with and without the bandpass filter. With the bandpass filter, illumination is restricted to a spectral region of λ = 1.7-2.4 μm. Infrared images taken from the PbS CQD/MoS_2/bP photodetector with (top) and without (bottom) the bandpass filter under (d) forward bias V_{DS} = 0.3 V (e) zero bias V_{DS} = 0 V, and (f) reverse bias V_{DS} = -0.3 V. Only under zero and reverse bias conditions is a full image obtainable with the band pass filter.

TOC figure

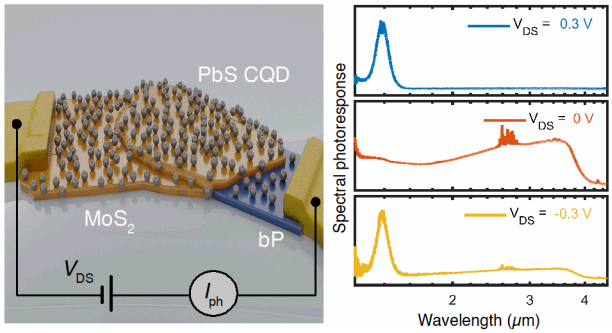
PbS CQD
MoS2
bP
VDS
Iph
Spectral photoresponse
VDS = 0.3 V
VDS = 0 V
VDS = -0.3 V
2
3
4
Wavelength (μm)